THE JOURNAL OF PHYSICAL CHEMISTRY LETTERS
A JOURNAL OF THE AMERICAN CHEMICAL SOCIETY

pubs.acs.org/JPCL Letter

Ultrafast Electron Dynamics in Coupled and Uncoupled HgTe Quantum Dots

S.G. Mizrahi,[#] M. Weis,[#] E. Péronne, A. Kies, A. Khalili, Y. Prado, S. Sauvage, E. Lhuillier, and D. Boschetto*

Cite This: *J. Phys. Chem. Lett.* 2024, 15, 12485−12493 Read Online

ACCESS | Metrics & More | Article Recommendations | Supporting Information

ABSTRACT: In this article, we study electron dynamics in HgTe quantum dots with a 1.9 μm gap, a material relevant for infrared sensing and emission, using ultrafast spectroscopy with 35 fs time resolution. Experiments have been carried out at several probing photon energies around the gap, which allows us to follow the relaxation path of the photoexcited electrons. We compare such dynamics in two kind of samples, HgTe quantum dots with long ligands and with short ligands, in order to distinguish the role of the coupling between adjacent quantum dots. Three main dynamics can be observed in the transient reflectivity on both samples, with slightly different relaxation times: two fast decays on the time scale of hundreds of femtoseconds and a few picoseconds, respectively, followed by a slower relaxation back to the unperturbed value over hundreds of picoseconds. The two fast components are associated with intraband relaxation of the photoexcited electrons within the conduction band, while the final relaxation path can be assigned to Auger relaxation mechanisms and to the slower interband exciton recombination.

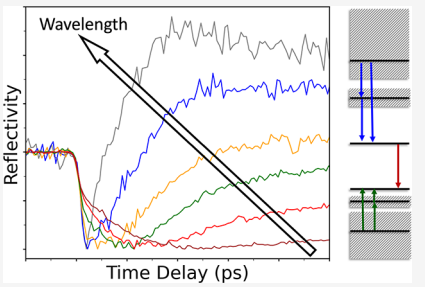

Semiconductor quantum dots (QDs) have strong potential for many applications to modern technologies, ranging from quantum information to energy harvesting.[1] By adjusting *ad hoc* the size of the nanocrystal, it is possible to play on the energy gap value in order to adapt it to a specific set of applications. For example, the energy gap plays a central rule in the use of quantum dots as emitter and/or detector in a given spectral range. In particular, HgTe quantum dots have been shown to have high potential for applications like light-emitting diodes (LEDs) and photodetectors in a broad spectral range, in particular by covering the short-wavelength infrared region (SWIR) up to the mid-infrared, from 1.2 to 5 μm.[2−5] The improvement of the efficiency of such devices relies on the understanding of the whole relaxation dynamics of out-of-equilibrium electrons in order to tackle and prevent dynamical competing processes. For example, the efficiency of light emission in semiconductor materials is intrinsically tied to the balance between their radiative and nonradiative relaxation rates. These rates, along with the nature of the emissive states (such as excitons, biexcitons, and trions), have been thoroughly explored in materials with wide band gaps.

However, our understanding remains significantly limited when it comes to the SWIR spectral region, where comprehensive studies still need an ongoing experimental effort. Previous works have demonstrated that holes and electrons have asymmetrical behaviors in bulk HgTe, as it has been shown through carrier mobility measurements.[6,7] These experiences suggest that the electron mobility is approximately 100 times greater than the hole mobility, a disparity that has been attributed to the stronger interaction of holes with the lattice.[8] This observation reflects significant asymmetry in the effective masses of holes and electrons. This asymmetry plays a crucial role in the relaxation processes within an isolated HgTe quantum dot, where it implies that hole relaxation occurs much more rapidly than electron relaxation. However, it is important to note that while electrons may exhibit higher mobility in bulk materials, this does not necessarily translate to higher mobility within quantum dots. In quantum dot films, charge transport is predominantly governed by hopping mechanisms, which can significantly alter the dynamics compared to those of bulk materials. Under strong excitation, multiexciton generation (MEG) occurs in HgTe quantum dots,[9−11] though the Auger effect may be reduced.[12] The identification of the relaxation channels as well as the measurement of the characteristic time scales is a mandatory step toward the improvement of devices for technological applications. While several studies have shown the transient dynamics in HgTe QDs, they were mostly focused on the long nanosecond range and trap dynamics in the microsecond to millisecond range,[13,14] tens of picoseconds dynamics,[12,15] or on subpicosecond time scales,[10] but without probing at the energy gap. Instead, only a few experiments probing at the energy gap with hundreds of femtoseconds time

Received: August 24, 2024
Revised: December 5, 2024
Accepted: December 5, 2024

https://doi.org/10.1021/acs.jpclett.4c02482
J. Phys. Chem. Lett. 2024, 15, 12485−12493

resolution exist,[9,16,17] despite their crucial role in understanding the dynamics of HgTe QDs, which is expected to be dominated by nonradiative processes.

In order to address this concern, we have investigated the electron dynamics of HgTe quantum dots with an emission wavelength at 1.9 μm with a time-resolution of 35 fs in a pump−probe configuration. The experiments have been performed by using a laser system delivering pulses centered at 800 nm at 1 kHz repetition rate, with a temporal duration of around 35 fs at full-width-at-half-maximum (fwhm), and energy/pulse of around 0.5 mJ. The laser beam was split into two arms: one arm was used as pump pulse at the central laser wavelength (800 nm, 1.55 eV), while the second arm passed through a parametric optical amplifier (OPA) in order to convert the wavelength in the SWIR spectral region. In this investigation, we have used an 800 nm pump pulse and selected the probe pulse wavelength in the range from 1.2 to 2.2 μm. The pump wavelength was selected to ensure electron photoexcitation well above the energy gap. On the other hand, the probing wavelength range allows us to depict a complete scenario of the energy relaxation channels of the photoexcited electrons within the quantum dots, as it covers from below to above the energy gap. The pump fluence has been kept in the range from 10 up to 80 μJ/cm^2. From the material thermal stability point of view, this range of fluences corresponds to a low excitation regime, as confirmed by the repeatability of the results after several long run measurements. A mechanical chopper is used to set the pump repetition rate at 0.5 kHz, and the signal of the reflected pulse is acquired by using a photodiode connected to a lock-in amplifier (model SR 830). The signal from the lock-in is detected at a master frequency of 0.5 kHz, in order to be sensitive only to pump induced reflectivity changes. This detection scheme has already been used in a number of investigations[3,4,18,19] as it allows to reach a very high signal-to-noise ratio. The same photodiode (InGaAs biased detector, model DET10D from ThorLabs, with a cutoff wavelength at 2.6 μm) is used in the whole spectral range, which ensures a reliable comparison between the different probing wavelengths.

The HgTe QDs used in this investigation have a lateral dimension below 10 nm (more details on the sample growth can be found in the Supporting Information). This size is chosen to match the desired band gap. Spectral characterization of the QDs samples has been carried out by a Fourrier transform infrared spectrometer (Thermo Fisher IS50r). Two types of samples were investigated, each with different ligands: one with a ligand length of 2 nm, referred to as uncoupled HgTe QDs, and the other with a ligand length of 0.5 nm, referred to as coupled HgTe QDs. In the uncoupled samples, we can assume that the electron wave function in a quantum dot does not overlap with that of another quantum dot, meaning the entire relaxation dynamics are expected to occur within a single quantum dot. In contrast, in the coupled sample, the electron relaxation process might involve multiple quantum dots. The absorbance of an uncoupled HgTe sample is shown in Figure 1 (upper panel) by a dark line. This behavior agrees with the established dependence of the energy band gap on the size of HgTe QDs.[20]

It is important to point out that the two types of ligands used here, dodecanethiol (DDT) and 3-mercaptopropionic acid (MPA) that capped the HgTe QDs, have similar dielectric properties due to their organic nature but differ in chain length. DDT provides a longer ligand length (≈ 2 nm), while MPA

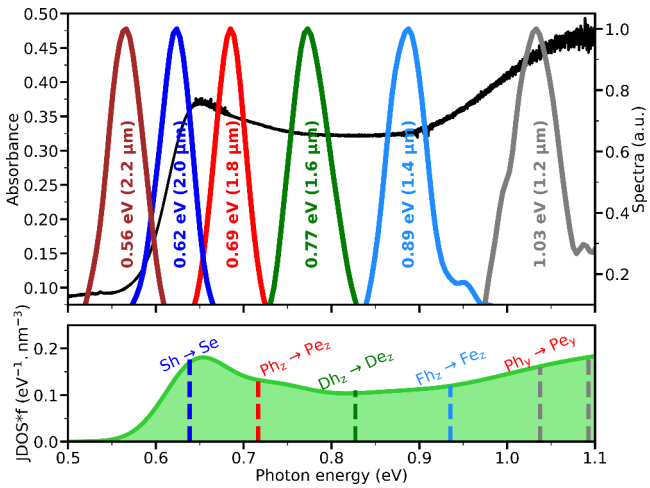

Figure 1. Characterization of the HgTe samples. Upper panel: Absorbance spectrum of the uncoupled HgTe sample (dark line) and the spectra of the selected probing wavelengths. Lower panel: Product of the calculated joint density of states (JDOS) and oscillator strength (f) for interband transitions (calculations are detailed in the Supporting Information).

offers a shorter one (≈ 0.5 nm). The thiol groups in both ligands ensure similar binding to the QD surface. The difference in chain length modulates the physical spacing and thus the electronic coupling between neighboring QDs. Considering that both ligands have comparable dielectric constants, the effect of dielectric confinement is minimal. Therefore, any variation in electron dynamics observed between the samples will be attributed primarily to differences in inter-QD coupling rather than dielectric effects.

We interpret the spectroscopy and dynamics measurements based on a simple picture of the electronic structure. The electronic structure is modeled to give an order of magnitude for the energies of the confined levels and oscillator strengths of interband and intraband transitions between these levels. We use a straightforward single band effective mass model, applied to a schematic cubic geometry with finite barrier heights and separation of the 3 directions following the reference work.[21] The volume, assuming an effective cubic shape, is to roughly mimic the overall and average confinement potentials of the observed tripod geometry of HgTe nanocrystals. To account for the strong nonparabolicity of the dispersion relation of bulk HgTe, an energy-dependent effective mass is considered, fitted around the Brillouin zone center to the dispersion calculated by a 14-bands $k\cdot p$ bulk HgTe model.[21,22] The computed energy spectrum is shown in Figure 2, as well as the eigenstates, from which we can calculate the oscillator strength of both intraband[23] and interband[24] (shown in Figure 1, lower panel) transitions between two eigenstates $|i\rangle$ and $|f\rangle$, of respective energies E_i and E_f:

$$f_{fi}^{intra} = \frac{2}{3m(E_f - E_i)} \sum_{x_j=x,y,z} |\langle f|\hat{p}_{x_j}|i\rangle|^2 \quad (1)$$

$$f_{fi}^{inter} = \frac{2|p_{cv}|^2}{m(E_f - E_i)} |\langle f|i\rangle|^2 \quad (2)$$

where f_{fi}^{intra} is the intraband oscillator strength averaged over the 3 electric field polarizations due to the assumed random orientation of the nanocrystals, f_{fi}^{inter} is the oscillator strength of

https://doi.org/10.1021/acs.jpclett.4c02482
J. Phys. Chem. Lett. 2024, 15, 12485−12493

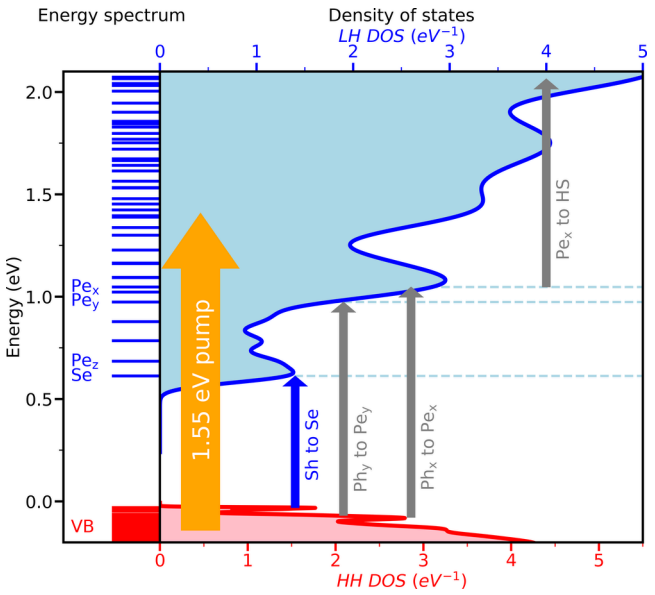

Figure 2. Calculated energy levels in HgTe QDs, as described in the text. The arrows indicate the allowed intra- and interband transitions.

the interband transition, respectively, m is the electron effective mass, $\hat{p}_{x_j}$ is the momentum operator along the direction x_j, and p_{cv} is the Kane momentum of transitions between the valence and conduction band (more information can be found in the Supporting Information). Although the cubic geometry differs significantly from the tripod geometry of the nanocrystals,[25] we expect and assume that the energy distribution and the calculated oscillator strength roughly follow the ones generated by the real volume confinement of the charge carriers.[26] The calculated energy levels are depicted in Figure 2.

The energy gap of the HgTe quantum dots is in the range of 1.9 μm (≈0.65 eV), corresponding to the first absorption feature in Figure 1 (upper panel). The width of this absorption feature is related to the size distribution of the quantum dots and the average homogeneous line width of the excitonic absorption, which can be estimated by using a Gaussian fit, from which we extract a fwhm of around 0.082 eV. Figure 1 (upper panel) also shows the spectra of the pulses used in transient reflectivity measurements, in order to compare them with the possible electronic inter- and intraband transitions. The main effect of the size distribution is the broadening of the overall state density, which defines a quasi-continuum of states. As it can be observed in Figure 2, the broadening creates a quasi-continuum in the higher energy states, while we can still distinguish the bottom level of the conduction band (S_e state), and the second level of the conduction band (P_e level).

Figure 3 shows the normalized transient reflectivity at various wavelengths around the gap, corresponding to those shown in Figure 1, for both uncoupled and coupled samples. Overall, the dynamics are dominated by three components, acting at three different time scales. Looking at the probing wavelength of 2 μm, we can observe a first sharp decrease, on a time scale of hundreds of femtoseconds, followed by a further decrease on a longer time scale of a few picoseconds, in agreement with previous studies.[3,9,27] Additionally, we observe that the time scale of this dynamic process differs between the two types of samples: approximately 3 ps for the uncoupled QDs and 2 ps for the coupled ones. The signal relaxes back following a double exponential-like increase in several hundreds of picoseconds, also in agreement with previous investigations.[12,28] In both types of samples, the most prominent difference appears when wavelengths are compared above and below 1.8 μm. For wavelengths $\lambda \geq 1.8$ μm, the sign of the reflectivity changes is always negative, corresponding essentially to a bleached absorption at any time delay. In contrast, for $\lambda < 1.8$ μm, the signal changes sign and becomes positive (i.e., photoinduced absorption) on a picosecond time scale. The most noticeable difference between the coupled and uncoupled QDs concerns the dynamics probed at 2 μm and below, while at longer wavelengths the signals show the same features. In coupled QDs, in addition to the shorter picosecond relaxation time scale, we observe a larger relative amplitude of the positive signal at 1.2 and 1.4 μm. We also remark that for both samples, the relaxations on a longer time scale overlap at 1.2, 1.4, and 1.6 μm, respectively.

To describe these behaviors, we must establish a link between the changes in absorption and the changes in reflectivity. This can be expressed, to a first-order approximation, as

$$\Delta R = \frac{\partial R}{\partial k}\Delta k + \frac{\partial R}{\partial n}\Delta n \tag{3}$$

where n and k represent the real and imaginary parts of the complex optical index, respectively. It is well-known that the absorbance α is proportional to k by the relation $\alpha = \frac{4\pi k}{\lambda}$. Since we are probing at wavelengths near the band gap, the optical properties are expected to be dominated by absorption processes (see Supporting Information for more details). Consequently, to explain the observed dynamical behavior, we will assume that within the measured wavelength range the changes in reflectivity are proportional to the changes in absorption, i.e., $\Delta R \propto \Delta\alpha$.

Let us first analyze the action of the pump pulse, keeping us aware of the approximations in the electronic structure model. The calculation of the oscillator strength shows that the pump pulse promotes the electrons from the F_h states below the top of the valence band to the quasi-continuum energy level states in the upper part of the conduction band (orange arrow in Figure 2). While thermalizing, the holes reach higher energy states at the top of the valence band. We note that because of the asymmetric hole/electron DOS, holes will thermalize faster and thus hole reach the top of valence band before electron reach the bottom of conduction band. This results in a lowering of the electrons occupation of the S_h state, which therefore decreases the absorption at a probing wavelength around $\lambda = 2$ μm, which leads to a decrease of the reflectivity accordingly to the experimental results. This process took around 250 fs. While the photoexcited electrons relax down to the bottom of the conduction band, namely to the S_e state, the transition $S_h \rightarrow S_e$ is further inhibited, decreasing even further the reflectivity. From the experiment, the time constant of this process is on the order of 3 ps for uncoupled QDs and 2 ps for the coupled ones. Other mechanisms that might slow down the relaxation process involve a hot-phonon bottleneck. However, further investigation is needed to disentangle the various mechanisms at play. Further electron relaxation on a longer time scale results from a combination of Auger and exciton recombinations. Beyond 5 ps and up to 100 ps, the Auger recombination dominates, in accordance with previous studies,[3,9,11] while exciton recombination dominates on a even longer time scale.

https://doi.org/10.1021/acs.jpclett.4c02482
J. Phys. Chem. Lett. 2024, 15, 12485−12493

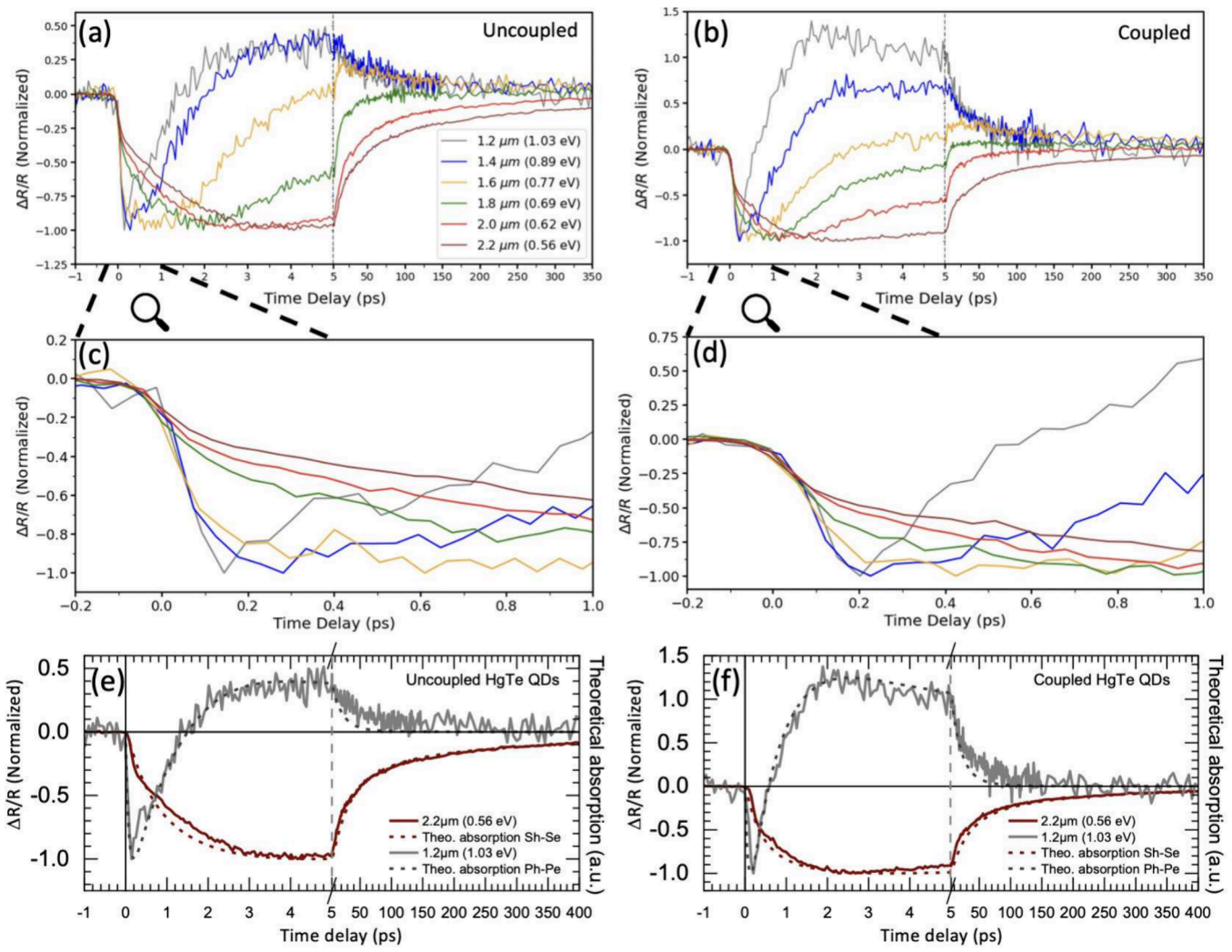

Figure 3. Normalized transient reflectivity for uncoupled (a) and coupled (b) HgTe QDs as a function of pump−probe time delay for different probing wavelengths. The pump pulse is centered at 800 nm, and the pump fluence is kept constant at 60 μJ/cm^2. (c) and (d) show a zoom of the experimental data from −0.2 to 1 ps for uncoupled and coupled HgTe QDs, respectively. The lower panel compares the experimental normalized reflectivity change (solid line) with the modeled transient absorption (dashed line) at 1.2 and 2.2 μm pump wavelengths for uncoupled (e) and coupled (f) HgTe QDs.

At shorter wavelength λ = 1.2 μm, the contribution of the main exciton $S_h \rightarrow S_e$ transition becomes negligible. The major contributions come from transitions promoting electrons from the P_h level and lower, to conductions states such as P_e and higher (that we will refer to as $P_h \rightarrow P_e$ for sake of simplicity), or from one of the three P_e states to upper states of the conduction band referred to as hot states (HS), as shown in Figure 2 by the transition $P_{e_x} \rightarrow HS$. The $P_e \rightarrow D_e$ transition would not only have a significant oscillator strength in the simplified cubic modeling of QDs, but also an oscillator strength larger than that of the $S_e \rightarrow P_e$ transition, due to the sum rule on intraband transitions and the altered asymmetric geometry, such as the tripod shape. We note here that at rest, before the pump pulse arrival, the transition $P_e \rightarrow HS$ is inhibited because there are no electrons in the P_e state (negligible sample self-doping). The situation changes after excitation by the pump pulse, which promotes electrons into higher energy states. The electrons empty the F_h states as described previously, reducing the absorption and, consequently, the reflectivity. However, while the electrons relax back to the S_e state at the bottom of the conduction band, the transition $P_e \rightarrow HS$ becomes possible, increasing the absorption and, therefore, the reflectivity with respect to the unperturbed state. The larger relative amplitude of the positive signal at 1.2 and 1.4 μm in coupled QDs further supports the notion that the increased number of relaxation channels in coupled QDs enhances the probability of photoexcited electrons reaching the lowest intermediate energy levels, such as the P states, before relaxing to the ground S states of the QD ensemble. Indeed, in coupled QDs, due to the electronic coupling between adjacent quantum dots, the individual electron states merge and spread out over multiple dots, resulting in the formation of extended states. This increases the density of states near the band edge. This higher density of states allows for a greater population of electrons in the S_e state and P_e states, enhancing the transition probability for the $P_e \rightarrow D_e$ like intraband transitions.

Furthermore, faster relaxation dynamics in coupled QDs, resulting from suppressed hot-phonon bottleneck effects and enhanced tunneling mechanisms, lead to a higher electron population at the low lying levels, such as the P_e levels. This higher population further amplifies the $\Delta R/R$ signal associated

https://doi.org/10.1021/acs.jpclett.4c02482
J. Phys. Chem. Lett. 2024, 15, 12485−12493

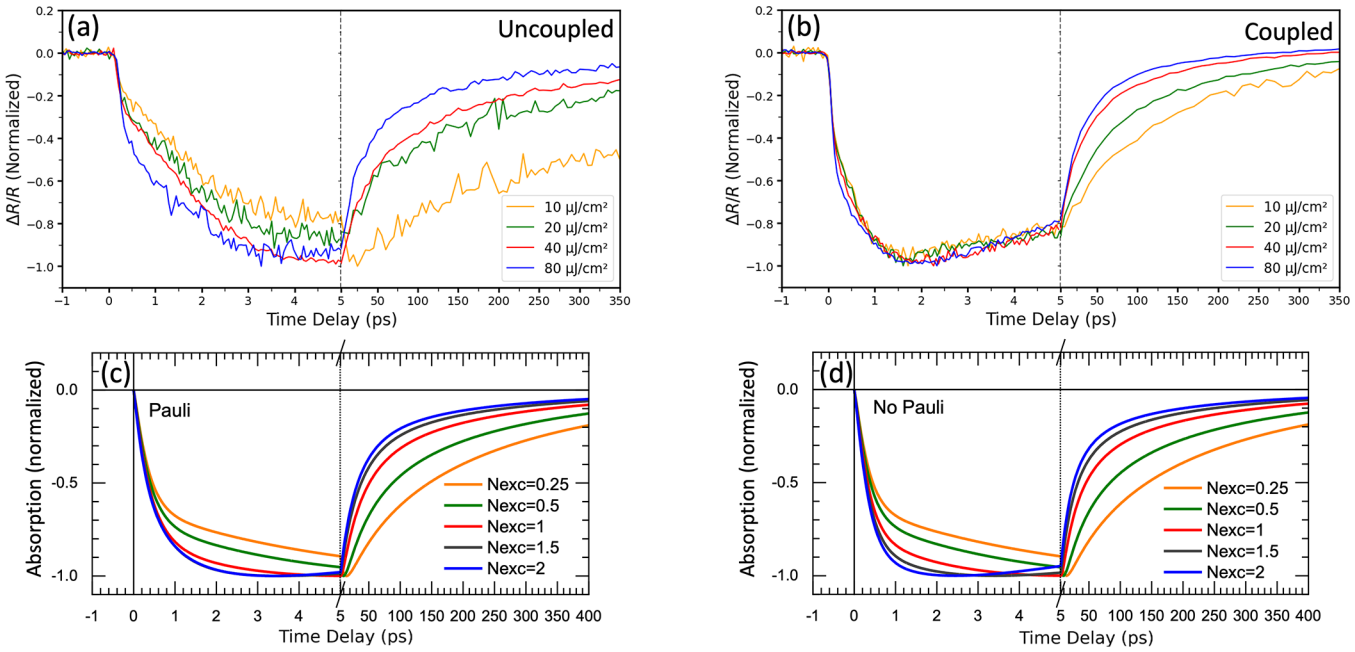

Figure 4. (a) Normalized transient reflectivity for uncoupled HgTe QDs at different pump fluences. The probe wavelength is 2 μm. (b) Same for the coupled QDs sample. (c) Transient differential absorption predicted by the rate equation model for coupled QDs, accounting for the Pauli exclusion principle in the ground electron (N_{e1}) and hole (N_{h1}) states. N_{exc} is the initial average exciton population per nanocrystal. (d) Predicted transient differential absorption for the same coupled QDs but with the Pauli exclusion principle removed from the rate equations.

with the $P_e \rightarrow HS$ transition. Therefore, the significant amplitude difference in the $\Delta R/R$ signal between coupled and uncoupled QDs arises from the combined effects of increased density redistribution of states, enhanced oscillator strength, broadened energy levels, and faster carrier relaxation dynamics in coupled QDs. These mechanisms tend to collectively enhance the $P_e \rightarrow D_e$ like transitions, leading to a stronger positive signal at 1.2 and 1.4 μm in coupled QDs.

Our interpretation is further supported by taking into account the energy decay rate estimated in ref 9. We can assume that the pump pulse promotes electrons to energy levels of approximately 1.4 eV above the valence band (as shown in Figure 2). To relax down to the conduction band (at 0.62 eV), these electrons must lose about 0.78 eV of energy. According to[9] the energy relaxation rate is approximately 0.36 eV/ps. This implies that the average relaxation time to the bottom of the conduction band is $\Delta\tau = \frac{0.78}{0.36} \approx 2.2$ ps. This aligns well with our interpretation, for which the positive variations probed at lower wavelengths arise from activation of the $P_e \rightarrow HS$ transition, reaching a plateau after 2 ps.

The relaxation rate of 0.36 eV/ps observed in HgTe quantum dots is indicative of efficient carrier relaxation dynamics. When compared to other quantum dot materials, such as PbS and PbSe, the relaxation rates reported are 0.65 eV/ps for PbS QDs[29] and range from 0.05 to 1.1 eV/ps for PbSe QDs.[30] This indicates that HgTe QDs exhibit relaxation rates that are comparable to those of these materials. These relaxation rates play a key role in applications involving carrier multiplication (CM), which is indeed a very promising way to improve optoelectronic and photovoltaic devices. The efficiency of CM processes is determined by the ability of high-energy carriers to generate additional electron−hole pairs before they relax to the band edge. A relaxation rate of 0.36 eV/ps suggests that HgTe QDs have a sufficiently rapid relaxation mechanism to facilitate CM. However, the CM efficiency in HgTe QDs might benefit from further tuning of the relaxation rates, potentially through modifications in QD size, surface ligands, or electronic coupling, to enhance the probability of multiple exciton generation before energy dissipation.

To gain deeper insight into the carrier dynamics, we performed an additional experiment by varying the pump fluence from 10 μJ/cm^2 to 80 μJ/cm^2, as shown in Figure 4, for a probing wavelength of 2 μm. For the coupled QDs, all of the curves exhibit similar behavior up to 5 ps, indicating identical relaxation times with respect to the number of pump photons. However, for longer time delays, we observe that the relaxation process accelerates with an increasing pump fluence. The transient reflectivity of uncoupled QDs shows a similar trend, though they exhibit slower relaxation time both at short, less than 5 ps, time scale and long, greater than 5 ps, time scales. This behavior is characteristic of Auger recombination processes, as previously reported in the literature.[3,9,17]

The two fast subpicosecond and below 5 ps components observed in the transient reflectivity measurements are attributed to intraband relaxation of photoexcited holes and electrons, respectively, within their respective bands. The final relaxation component, with a time scale of approximately 100 ps, is assigned to interband Auger recombination processes, while we expect the exciton recombination to take place on a much longer time scale. This assignment is supported by the relaxation time scale, which is consistent with reported Auger recombination rates in similar semiconductor quantum dots.[11] Furthermore, previous studies on HgTe QDs have associated this time scale with interband Auger recombination.[9,10,12] Additionally, the fluence-dependent acceleration of relaxation dynamics suggests the involvement of multiexciton interactions, a characteristic feature of Auger processes.

It is important to note that Auger recombination in HgTe QDs may differ from that in other QDs, such as CdSe QDs,

https://doi.org/10.1021/acs.jpclett.4c02482
J. Phys. Chem. Lett. 2024, 15, 12485−12493

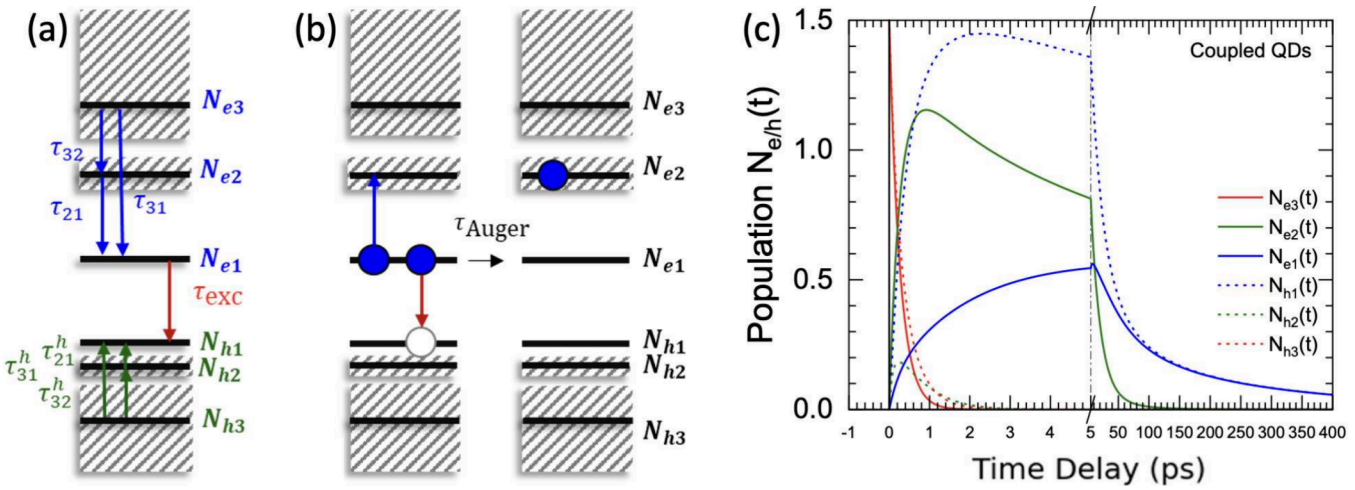

Figure 5. (a) Schematic of the intraband and interband dynamics between the energy levels commented in the main text, except from the Auger processes. (b) Three-particule Auger exciton recombination mechanism added to the model, where the blue disks represent electrons and the white disk represents one hole. (c) Occupation of energy level versus pump−probe time delay, extracted from the best fit of the coupled HgTe QDs parameter set. The calculation is made by using the rate equation explained in the main text.

due to differences in their electronic structure and density of states. Specifically, HgTe QDs exhibit a higher DOS for holes compared to electrons, enhancing the probability of multi-exciton interactions and facilitating Auger recombination. In contrast, for example, CdSe QDs generally display a more balanced DOS between electrons and holes, which influences the relaxation dynamics differently. While our current study suggests that the ≈5−100 ps time-scale dynamics is driven by the interband Auger relaxation process, further investigations are needed to fully elucidate this contribution. For example, time-resolved photoluminescence or selective pump−probe spectroscopy targeting hole dynamics could provide more direct evidence of the role of interband Auger recombination in HgTe QDs. Below, we present fitted simulations supporting such a mechanism.

The situation becomes more intriguing in the case of uncoupled QDs at shorter time scales, below 5 ps. Specifically, the ratio of the amplitude between the initial dynamics (on a 100 fs time scale) and the picosecond dynamics clearly depends on the pump fluence. At a low pump fluence, the amplitude of the initial drop is significantly reduced relative to the second phase of the dynamics.

To better understand the reflectivity dynamics, we employed a rate equation model to fit the data. The aim of our approach is to keep the model as simple as possible, while capturing the main features of the measurements. Namely, the model aims at accounting simultaneously—with a fixed set of parameters for each sample—for (1) the time dependence over the 0−400 ps time scale; (2) the behavior at the wavelengths 1.2 and 2.2 μm; (3) the normalized and relative reflectivity amplitude changes; and (4) the effect of the pump fluence on reflectivity at 2 μm. For simplicity, we consider only three energy pseudolevels in the conduction band and symmetrically three pseudolevels in the valence band. The relaxation scheme is described in Figure 5(a). These pseudolevels are chosen to represent the group of states that roughly rules the intraband and interband absorption and the relaxation of charge carriers, as represented by downward arrows in the conduction band and upward arrow in the valence bands. The model considers the ground states N_{e1} and N_{h1} of both conduction and valence band, respectively, where the electron and hole relax relatively fast before the slower excitonic recombination. N_{e2} and N_{h2} group together intermediate states such as the *P*-like intermediate states exhibiting an expected strong theoretical absorption toward the *D*-states. N_{e2} and N_{h2} also include states that contributes to the relaxation toward the ground S_e and S_h states. Finally, the model assembles into N_{e3} and N_{h3} all of the numerous high energy states (referred to as hot states (HS)), in particular optically pumped by the pump pulse. The model involves twice 3 relaxation times for intraband relaxation (conduction and valence bands) plus one interband recombination time for the exciton. We voluntarily neglect the slow radiative and nonradiative recombination between excited states like N_{e2}-N_{h2} and N_{e3}-N_{h3}. In order to account for the Auger effect, however, we consider an additional Auger recombination process as described in the Supporting Information, Section VI. Lastly, the model accounts for the Pauli blocking of carrier relaxation only toward the ground levels N_{e1} and N_{h1} assuming a degeneracy of 2 for these two levels. Note that the level populations N_i are considered as averages over the probed nanocrystal ensemble and are hence real (noninteger) positive numbers.

Under these assumptions, the rate equations, described in more detail in the Supporting Information, are given by

$$\frac{dN_{e3}(t)}{dt} = -\frac{\left(1-\frac{N_{e1}(t)}{2}\right)N_{e3}(t)}{\tau_{31}} - \frac{N_{e3}(t)}{\tau_{32}} \tag{4}$$

$$\frac{dN_{e2}(t)}{dt} = \frac{N_{e1}(t)^2 N_{h1}(t)}{2\tau_{Auger}} - \frac{\left(1-\frac{N_{e1}(t)}{2}\right)N_{e2}(t)}{\tau_{21}} + \frac{N_{e3}(t)}{\tau_{32}} \tag{5}$$

$$\frac{dN_{e1}(t)}{dt} = -\frac{N_{e1}(t)^2 N_{h1}(t)}{\tau_{Auger}} - \frac{\sqrt{N_{e1}(t)N_{h1}(t)}}{\tau_{exc}} + \frac{\left(1-\frac{N_{e1}(t)}{2}\right)N_{e2}(t)}{\tau_{21}} + \frac{\left(1-\frac{N_{e1}(t)}{2}\right)N_{e3}(t)}{\tau_{31}} \tag{6}$$

https://doi.org/10.1021/acs.jpclett.4c02482
J. Phys. Chem. Lett. 2024, 15, 12485−12493

Table 1. Fixed Sets of Relaxation Times Used in the Rate Equation Model for Uncoupled and Coupled QDs, with N_{exc} = 1.5

Relaxation times (ps)	τ_{e32}	τ_{e31}	τ_{e21}	τ_{h21}	τ_{h31}	τ_{h32}	τ_{Auger}	τ_{exc}	α_{PD}
Uncoupled	0.6 ps	10 ps	6 ps	0.08 ps	1.7 ps	0.8 ps	5 ps	750 ps	1.045
Coupled	0.3 ps	2 ps	6 ps	0.1 ps	0.6 ps	0.55 ps	5 ps	300 ps	1.13

$$\frac{dN_{h1}(t)}{dt} = -\frac{N_{e1}(t)^2 N_{h1}(t)}{2\tau_{\text{Auger}}} - \frac{\sqrt{N_{e1}(t)N_{h1}(t)}}{\tau_{\text{exc}}} + \frac{\left(1-\frac{N_{h1}(t)}{2}\right)N_{h2}(t)}{\tau_{\text{h21}}} + \frac{\left(1-\frac{N_{h1}(t)}{2}\right)N_{h3}(t)}{\tau_{\text{h31}}} \quad (7)$$

$$\frac{dN_{h2}(t)}{dt} = \frac{N_{h3}(t)}{\tau_{\text{h32}}} - \frac{\left(1-\frac{N_{h1}(t)}{2}\right)N_{h2}(t)}{\tau_{\text{h21}}} \quad (8)$$

$$\frac{dN_{h3}(t)}{dt} = -\frac{\left(1-\frac{N_{h1}(t)}{2}\right)N_{h3}(t)}{\tau_{\text{h31}}} - \frac{N_{h3}(t)}{\tau_{\text{h32}}} \quad (9)$$

along with the initial conditions, $N_{e3}(t=0) = N_{h3}(t=0) = N_{exc}$ and $N_{e2}(t=0) = N_{e1}(t=0) = N_{h1}(t=0) = N_{h2}(t=0) = 0$, where N_{exc} is the average number of photoexcited excitons per nanocrystal by the initial pump pulse (N_{exc} = 1.5, unless otherwise specified). We use an initial condition rather than a time-dependent source term in the equations, because the pump pulse is assumed to be much shorter than all other relevant relaxation times. We note that the sum of all equations reduces to the sum of the interband recombination mechanisms and that the number of electrons, $N_{e1} + N_{e2} + N_{e3}$, equals the number of holes, $N_{h1} + N_{h2} + N_{h3}$, at all times $t \geq 0$ as shown in Figure S5 of the Supporting Information. We assume that each QD is excited by an average number of excitons N_0 from the pump pulse. Additionally, we assume that we probe the absorption of the QD ensemble linearly near the energy gap, as described by the following:

$$\Delta R \propto [-(N_{e1}(t) - N_{e1}(0)) - (N_{h1}(t) - N_{h1}(0))] \quad (10)$$

and near the $P_h \rightarrow P_e$ transition at higher energy following:

$$\Delta R \propto [-(N_{e2}(t) - N_{e2}(0)) - (N_{h2}(t) - N_{h2}(0))] + \alpha_{PD} N_{e2}(t) \quad (11)$$

where $\alpha_{PD} \approx 1$ is the adjustable relative absorption coefficient of the $P_e \rightarrow D_e$ intraband transitions as compared to the interband transition. Note that we assume there is no intraband absorption for low-energy probe photons around the $S \rightarrow P$ transition, as this transition is out of resonance with the probe. Additionally, the optical response of the $P_e \rightarrow D_e$ transition is evaluated solely from the N_{e2} population (absorption), and not from the N_{e3} population (stimulated emission), since this N_{e3} pseudolevel includes other nonoptically active states and is depleted much more quickly than N_{e2}.

The fitting curves using this model for the 60 μJ/cm^2 fluence are shown in Figures 3(e) and 3(f) for the uncoupled and coupled QDs samples, respectively. For both samples and thus for the single set of parameters given in Table 1, the model agrees reasonably well with the experimental data for time delays below 5 ps, although it fits the coupled QDs better than the uncoupled QDs. Beyond 5 ps, the model captures the biexponential relaxation, though it tends to underestimate the residual absorption amplitude at longer time scales, as also shown in Figure S4 of the Supporting Information in both non-normalized linear and logarithmic scales. In Table 1, one notes that the relaxation times are significantly shorter for the coupled quantum dot parameter set than for the uncoupled one, as expected and discussed earlier.

This model also qualitatively describes the fluence dependence, as shown in Figure 4(c). However, it fails to closely reproduce the fluence dependence for the coupled QDs. Figure 4(d) shows the reflectivity dynamics calculated by removing the Pauli blocking terms in the rate equations, using the same parameter set as that in Figure 4(c). Removing the Pauli terms corresponds to assuming that the carriers can find nearby free relaxation states by tunneling to adjacent QDs. At first glance, the theoretical dynamics occur over significantly shorter times than those observed experimentally. However, the nearly identical dynamics observed experimentally in the coupled QDs sample for times shorter than 5 ps seem counterintuitive, as the calculation predicts a strong dependence on the pump fluence. The fact that this model works better for uncoupled QDs than for coupled ones suggests a missing factor in the model that plays a significant role in the early stages of the dynamics. One possible explanation is the lack of dependence on electron and lattice temperatures, which are known to influence transient dynamics.[18,31,32] Indeed, electron−phonon coupling, which drives intraband electron relaxation, strongly depends on both the electron and lattice temperatures. Such nonradiative processes transfer energy to the vibrational modes of the lattice and to the ligands through nonadiabatic interactions.[30,33] These additional pathways contribute to the gradual return of the system to the ground state without photon emission.[34] The complexity introduced by different ligand environments and inter-QD coupling further highlights the need to consider multiple sources of the long-lived signal. Further investigations should address the impact of thermal effects on the dynamics of the QDs.

Figure 5c presents the calculated level populations as a function of time delay, fitted for the coupled sample, which exhibits a stronger reflectivity sign change. The calculation shows that at low energy, corresponding to the intermediate and ground states, relaxation occurs much faster in the valence band than in the conduction band, likely due to the higher density of states in the valence band, as observed more clearly in Figure S3. Furthermore, the calculation indicates that the strong population of the N_{e2} pseudolevel and its related intraband $P \rightarrow D$ absorption can explain the surprising experimental change in the reflectivity variation sign, which compensates for and eventually surpasses the bleaching of the interband absorption, as shown in Figure 3.

In conclusion, we have characterized the time scales of the main electronic transitions that dominate the transient reflectivity response of HgTe quantum dots by probing the sample at various wavelengths around the energy gap with femtosecond time resolution. By calculating the oscillator strength of each transition, we were able to assign specific parts of the relaxation dynamics to distinct intra- and interband transitions, particularly those involving the S_e and P_e states.

https://doi.org/10.1021/acs.jpclett.4c02482
J. Phys. Chem. Lett. 2024, 15, 12485−12493

Our comparison between samples with short and long ligands revealed faster relaxation dynamics in the coupled QDs compared to the uncoupled QDs. This is consistent with the fact that in coupled QDs, the wave function overlaps with surrounding QDs, leading to an increase in the available relaxation channels. A simple rate equation model was employed to describe the experimental dynamical behavior across most fluences for both types of samples. However, the dynamics of coupled QDs as a function of the pump fluence exhibit a significant deviation from the simulated behavior, indicating the need to include an additional factor in the model at the early stage of the dynamics. This could involve considering transient electron and lattice temperatures, as these can affect electron−phonon coupling, which in turn influences electron intraband transitions. Further experimental investigations are required to clarify the contribution of other relaxation channels and thermal parameters. Additional experimental techniques, such as transient dielectric function dynamics[35,36] or time-resolved electron diffraction,[37,38] will help disentangle the contributions of all the degrees of freedom in the crystal to the overall dynamics.

■ ASSOCIATED CONTENT

Supporting Information

The Supporting Information is available free of charge at https://pubs.acs.org/doi/10.1021/acs.jpclett.4c02482.

Samples preparation, electronic structure calculations, relative change in reflectivity at a resonant transition, computation of the average number of absorbed photons per QD, transient reflectivity, modeling of the electron and hole dynamics, and experimental reflectivity measurements without normalization (PDF)

■ AUTHOR INFORMATION

Corresponding Author

D. Boschetto − *Laboratoire d'Optique Appliquée, ENSTA Paris, CNRS, Ecole Polytechnique, Institut Polytechnique de Paris, 91761 Palaiseau, France;* orcid.org/0000-0001-6516-0652; Email: davide.boschetto@ensta.fr

Authors

S.G. Mizrahi − *Laboratoire d'Optique Appliquée, ENSTA Paris, CNRS, Ecole Polytechnique, Institut Polytechnique de Paris, 91761 Palaiseau, France;* orcid.org/0000-0002-7450-4346

M. Weis − *Laboratoire d'Optique Appliquée, ENSTA Paris, CNRS, Ecole Polytechnique, Institut Polytechnique de Paris, 91761 Palaiseau, France*

E. Péronne − *Laboratoire d'Optique Appliquée, ENSTA Paris, CNRS, Ecole Polytechnique, Institut Polytechnique de Paris, 91761 Palaiseau, France;* orcid.org/0000-0002-8845-0414

A. Kies − *Laboratoire d'Optique Appliquée, ENSTA Paris, CNRS, Ecole Polytechnique, Institut Polytechnique de Paris, 91761 Palaiseau, France*

A. Khalili − *Sorbonne Université, CNRS, Institut des NanoSciences de Paris, 75005 Paris, France;* orcid.org/0000-0001-5685-9963

Y. Prado − *Sorbonne Université, CNRS, Institut des NanoSciences de Paris, 75005 Paris, France;* orcid.org/0000-0001-6228-2486

S. Sauvage − *C2N, Centre de Nanosciences et de Nanotechnologies, Université Paris-Saclay, CNRS, 91120 Palaiseau, France;* orcid.org/0000-0001-8132-1372

E. Lhuillier − *Sorbonne Université, CNRS, Institut des NanoSciences de Paris, 75005 Paris, France;* orcid.org/0000-0003-2582-1422

Complete contact information is available at: https://pubs.acs.org/10.1021/acs.jpclett.4c02482

Author Contributions

#(S.G.M. and M.W.) These authors contributed equally to this work.

Notes

The authors declare no competing financial interest.

■ ACKNOWLEDGMENTS

This work was supported by French state funds managed by the ANR grants: Frontal (ANR-19-CE09-0017), TOCYDYS (ANR-19-CE30-0015-03), Copin (ANR-19-CE24-0022), Bright (ANR-21-CE24-0012), MixDFerro (ANR-21-CE09-0029), and Quicktera (ANR-22-CE09-0018). We also acknowledge the support from the Region Ile-de-France in the framework of the SESAME Electrophonon project (grant no. 14014520), the French department of defense (DGA), and the ERC grant AQDtive (grant no. 101086358).

■ REFERENCES

(1) García de Arquer, F. P.; Talapin, D. V.; Klimov, V. I.; Arakawa, Y.; Bayer, M.; Sargent, E. H. Semiconductor quantum dots: Technological progress and future challenges. *Science* **2021**, *373* (6555), No. eaaz8541.

(2) Keuleyan, S.; Lhuillier, E.; Guyot-Sionnest, P. Synthesis of colloidal hgte quantum dots for narrow mid-ir emission and detection. *J. Am. Chem. Soc.* **2011**, *133*, 16422−16424.

(3) Qu, J.; Weis, M.; Izquierdo, E.; Mizrahi, S. G.; Chu, A.; Dabard, C.; Gréboval, C.; Bossavit, E.; Prado, Y.; Péronne, E.; Ithurria, S.; Patriarche, G.; Silly, M. G.; Vincent, G.; Boschetto, D.; Lhuillier, E. Electroluminescence from nanocrystals above 2 μm. *Nat. Photonics* **2022**, *16*, 38−44.

(4) Khalili, A.; Weis, M.; Mizrahi, S. G.; Chu, A.; Dang, T. H.; Abadie, C.; Gréboval, C.; Dabard, C.; Prado, Y.; Xu, X. Z.; Péronne, E.; Livache, C.; Ithurria, S.; Patriarche, G.; Ramade, J.; Vincent, G.; Boschetto, D.; Lhuillier, E. Guided-mode resonator coupled with nanocrystal intraband absorption. *ACS Photonics* **2022**, *9*, 985−993.

(5) Shen, X.; Peterson, J. C.; Guyot-Sionnest, P. Mid-infrared hgte colloidal quantum dot leds. *ACS Nano* **2022**, *16* (5), 7301−7308.

(6) Byszewski, P.; Dziuba, E. Z.; Gałązka, R. R.; Szlenk, K.; Szymborski, K.; Walukiewicz, W. Magnetic-field-induced energy gap in hgte observed in transport measurements. *physica status solidi (b)* **1975**, *71*, 117−124.

(7) Dziuba, Z.; Wróbel, J. The Mobility of Electrons and Holes in HgTe in the Temperature Range of Intrinsic Conduction. *physica status solidi (b)* **1980**, *100*, 379−387.

(8) Malyk, O. Nonelastic charge carrier scattering in mercury telluride. *J. Alloys Compd.* **2004**, *371*, 146−149.

(9) Ruppert, M.; Bui, H.; Sagar, L. K.; Geiregat, P.; Hens, Z.; Bester, G.; Huse, N. Intraband dynamics of mid-infrared HgTe quantum dots. *Nanoscale* **2022**, *14*, 4123−4130.

(10) Al-Otaify, A.; Kershaw, S. V.; Gupta, S.; Rogach, A. L.; Allan, G.; Delerue, C.; Binks, D. J. Multiple exciton generation and ultrafast exciton dynamics in HgTe colloidal quantum dots. *Phys. Chem. Chem. Phys.* **2013**, *15* (39), 16864.

(11) Melnychuk, C.; Guyot-Sionnest, P. Multicarrier dynamics in quantum dots. *Chem. Rev.* **2021**, *121* (4), 2325−2372.

(12) Melnychuk, C.; Guyot-Sionnest, P. Slow auger relaxation in hgte colloidal quantum dots. *J. Phys. Chem. Lett.* **2018**, *9* (9), 2208−2211.
(13) Martinez, B.; Livache, C.; Goubet, N.; Jagtap, A.; Cruguel, H.; Ouerghi, A.; Lacaze, E.; Silly, M. G.; Lhuillier, E. Probing charge carrier dynamics to unveil the role of surface ligands in hgte narrow band gap nanocrystals. *J. Phys. Chem. C* **2018**, *122* (1), 859−865.
(14) Qu, J.; Rastogi, P.; Gréboval, C.; Lagarde, D.; Chu, A.; Dabard, C.; Khalili, A.; Cruguel, H.; Robert, C.; Xu, X. Z.; Ithurria, S.; Silly, M. G.; Ferré, S.; Marie, X.; Lhuillier, E. Electroluminescence from hgte nanocrystals and its use for active imaging. *Nano Lett.* **2020**, *20* (8), 6185−6190.
(15) Qu, J.; Rastogi, P.; Gréboval, C.; Lagarde, D.; Chu, A.; Dabard, C.; Khalili, A.; Cruguel, H.; Robert, C.; Xu, X. Z.; Ithurria, S.; Silly, M. G.; Ferré, S.; Marie, X.; Lhuillier, E. Electroluminescence from hgte nanocrystals and its use for active imaging. *Nano Lett.* **2020**, *20* (8), 6185−6190.
(16) Sergeeva, K. A.; Fan, K.; Sergeev, A. A.; Hu, S.; Liu, H.; Chan, C. C.; Kershaw, S. V.; Wong, K. S.; Rogach, A. L. Ultrafast charge carrier dynamics and transport characteristics in hgte quantum dots. *J. Phys. Chem. C* **2022**, *126* (45), 19229−19239.
(17) Fan, K.; Sergeeva, K. A.; Sergeev, A. A.; Zhang, L.; Chan, C. C. S.; Li, Z.; Zhong, X.; Kershaw, S. V.; Liu, J.; Rogach, A. L.; Wong, K. S. Slow hot-exciton cooling and enhanced interparticle excitonic coupling in hgte quantum dots. *ACS Nano* **2024**, *18* (27), 18011−18021.
(18) Boschetto, D.; Gamaly, E. G.; Rode, A. V.; Luther-Davies, B.; Glijer, D.; Garl, T.; Albert, O.; Rousse, A.; Etchepare, J. Small Atomic Displacements Recorded in Bismuth by the Optical Reflectivity of Femtosecond Laser-Pulse Excitations. *Phys. Rev. Lett.* **2008**, *100*, 027404.
(19) Servol, M.; Moisan, N.; Collet, E.; Cailleau, H.; Kaszub, W.; Toupet, L.; Boschetto, D.; Ishikawa, T.; Moréac, A.; Koshihara, S.; Maesato, M.; Uruichi, M.; Shao, X.; Nakano, Y.; Yamochi, H.; Saito, G.; Lorenc, M. Local response to light excitation in the charge-ordered phase of $(EDO\text{-}TTF)_2Sbf_6$. *Phys. Rev. B* **2015**, *92*, 024304.
(20) Greboval, C.; Chu, A.; Goubet, N.; Livache, C.; Ithurria, S.; Lhuillier, E. Mercury chalcogenide quantum dots: Material perspective for device integration. *Chem. Rev.* **2021**, *121* (7), 3627−3700.
(21) Harrison, P.; Valavanis, A. *Quantum wells, wires and dots: theoretical and computational physics of semiconductor nanostructures*; Wiley, Hoboken, NJ, USA, fourth ed., 2016.
(22) Moghaddam, N.; Gréboval, C.; Qu, J.; Chu, A.; Rastogi, P.; Livache, C.; Khalili, A.; Xu, X. Z.; Baptiste, B.; Klotz, S.; Fishman, G.; Capitani, F.; Ithurria, S.; Sauvage, S.; Lhuillier, E. The Strong Confinement Regime in HgTe Two-Dimensional Nanoplatelets. *J. Phys. Chem. C* **2020**, *124*, 23460−23468.
(23) Wooten, F. *Optical properties of solids*; Academic Press, New York, 1972.
(24) Alén, B.; Bosch, J.; Granados, D.; Martínez-Pastor, J.; García, J. M.; González, L. Oscillator strength reduction induced by external electric fields in self-assembled quantum dots and rings. *Phys. Rev. B* **2007**, *75*, 045319.
(25) Chee, S.-S.; Gréboval, C.; Magalhaes, D. V.; Ramade, J.; Chu, A.; Qu, J.; Rastogi, P.; Khalili, A.; Dang, T. H.; Dabard, C.; Prado, Y.; Patriarche, G.; Chaste, J.; Rosticher, M.; Bals, S.; Delerue, C.; Lhuillier, E. Correlating structure and detection properties in hgte nanocrystal films. *Nano Lett.* **2021**, *21* (10), 4145−4151.
(26) Allan, G.; Delerue, C. Tight-binding calculations of the optical properties of HgTe nanocrystals. *Phys. Rev. B* **2012**, *86*, 165437.
(27) Apretna, T.; Massabeau, S.; Gréboval, C.; Goubet, N.; Tignon, J.; Dhillon, S.; Carosella, F.; Ferreira, R.; Lhuillier, E.; Mangeney, J. Few picosecond dynamics of intraband transitions in thz hgte nanocrystals. *Nanophotonics* **2021**, *10* (10), 2753−2763.
(28) Keuleyan, S.; Kohler, J.; Guyot-Sionnest, P. Photoluminescence of Mid-Infrared HgTe Colloidal Quantum Dots. *J. Phys. Chem. C* **2014**, *118*, 2749−2753.
(29) Cho, B.; Peters, W. K.; Hill, R. J.; Courtney, T. L.; Jonas, D. M. Bulklike Hot Carrier Dynamics in Lead Sulfide Quantum Dots. *Nano Lett.* **2010**, *10*, 2498−2505.
(30) Schaller, R. D.; Pietryga, J. M.; Goupalov, S. V.; Petruska, M. A.; Ivanov, S. A.; Klimov, V. I. Breaking the Phonon Bottleneck in Semiconductor Nanocrystals via Multiphonon Emission Induced by Intrinsic Nonadiabatic Interactions. *Phys. Rev. Lett.* **2005**, *95*, 196401.
(31) Sielcken, H. J.; Bakker, H. J. Probing the ultrafast electron and lattice dynamics of gold using femtosecond mid-infrared pulses. *Phys. Rev. B* **2020**, *102*, 134301.
(32) Lejman, M.; Weis, M.; Nilforoushan, N.; Faure, J.; Ta Phuoc, V.; Cario, L.; Boschetto, D. Ultrafast photoinduced conductivity reduction by bonding orbital control in an incommensurate crystal. *Phys. Rev. B* **2023**, *108*, 134306.
(33) Cooney, R. R.; Sewall, S. L.; Dias, E. A.; Sagar, D. M.; Anderson, K. E. H.; Kambhampati, P. Unified picture of electron and hole relaxation pathways in semiconductor quantum dots. *Phys. Rev. B* **2007**, *75*, 245311.
(34) Lim, J.; Choi, Y. C.; Choi, D.; Chang, I.-Y.; Hyeon-Deuk, K.; Jeong, K. S.; Kwak, K.; Cho, M. Ultrafast intraband Auger process in self-doped colloidal quantum dots. *Matter* **2021**, *4*, 1072−1086.
(35) Boschetto, D.; Garl, T.; Rousse, A. Ultrafast dielectric function dynamics in bismuth. *Journal of Modern Optics* **2010**, *57* (11), 953−958.
(36) Thiemann, F.; Sciaini, G.; Kassen, A.; Lott, T. S.; Horn-von Hoegen, M. Disentangling the electronic and lattice contributions to the dielectric response of photoexcited bismuth. *Phys. Rev. B* **2024**, *109*, L041105.
(37) González Vallejo, I.; Gallé, G.; Arnaud, B.; Scott, S. A.; Lagally, M. G.; Boschetto, D.; Coulon, P.-E.; Rizza, G.; Houdellier, F.; Le Bolloc'h, D.; Faure, J. Observation of large multiple scattering effects in ultrafast electron diffraction on monocrystalline silicon. *Phys. Rev. B* **2018**, *97*, 054302.
(38) Badali, D. S.; Gengler, R. Y. N.; Miller, R. J. D. Ultrafast electron diffraction optimized for studying structural dynamics in thin films and monolayers. *Structural Dynamics* **2016**, *3*, 034302.

https://doi.org/10.1021/acs.jpclett.4c02482
J. Phys. Chem. Lett. 2024, 15, 12485−12493

Supporting information for

Ultrafast electron dynamics in coupled and uncoupled HgTe quantum dots

S.G. Mizrahi†,[1] M. Weis†,[1] E. Péronne,[1] A. Kies,[1] A. Khalili,[2] Y. Prado,[2] S. Sauvage,[3] E. Lhuillier,[2] and D. Boschetto*[1]

[1]*Laboratoire d'Optique Appliquée, ENSTA Paris, CNRS, Ecole Polytechnique, Institut Polytechnique de Paris, 91761 Palaiseau, France*

[2]*Sorbonne Université, CNRS, Institut des NanoSciences de Paris, 4 place jussieu, 75005 Paris, France*

[3]*C2N, Centre de Nanosciences et de Nanotechnologies, Université Paris-Saclay, CNRS, 91120 Palaiseau, France*

(Dated: December 5, 2024)

I. SAMPLES PREPARATION

Chemicals: Mercury chloride ($HgCl_2$, Sigma-Aldrich, 99%), tellurium powder (Te, Sigma-Aldrich, 99.99%), trioctylphosphine (TOP, Alfa, 90%), oleylamine (OLA, Acros, 80-90%), dodecanethiol (DDT, Sigma-Aldrich, 98%), 2-mercaptoethanol (MPOH, Merck, >99%), and N,N dimethylformamide (DMF, VWR), toluene (VWR, 99.8%) were used. All chemicals were used without further purification, except oleylamine that is centrifuged before use. **Mercury compounds are highly toxic. Handle them with special care.**

1 M TOP:Te precursor: 2.54 g of Te powder was mixed with 20 mL of TOP in a three-neck flask. The flask was kept under vacuum at room temperature for 5 min before the temperature was raised to 100°C. Degassing was conducted at this temperature for 20 min. Next, the atmosphere was switched to N_2 and the temperature was raised to 275°C. The solution was stirred until a clear orange coloration was obtained. The flask was then cooled down to room temperature and the color turned to yellow. Finally, this solution was transferred to a nitrogen-filled glove box for storage.

HgTe nanocrystals emitting at 2 μm: In a 100 mL three neck flask, 543 mg of $HgCl_2$ and 50 mL of oleylamine were degassed under vacuum at 110°C for 1 h. Meanwhile, 2 mL of TOP:Te (1 M) were extracted from the glove box and mixed with 8 mL of oleylamine. After that the atmosphere was switched to N_2 and the temperature was set as 70°C. When the temperature stabilized, the TOP:Te solution was quickly injected. After 3 min of reaction, 10 mL of DDT/Toluene (1:9 in volume) solution was injected and a water bath was used to quench the reaction. The nanocrystals were precipitated with methanol and redispersed in $CHCl_3$ twice. After that, the nanocrystals dispersed in $CHCl_3$ were centrifugated to remove the unstable phase. The stable phase was precipitated again with methanol and stored in toluene.

HgTe ink preparation: 10 mg of $HgCl_2$, 2 mL of MPOH, and 18 mL of DMF are mixed to form an exchange solution. 0.25 mL of this exchange solution and 0.5 mL of DMF are added to 0.25 mL of HgTe NCs in toluene. Phase dissociation occurs when a few drops of hexane are added to the mixture: the dark bottom phase is where the NCs migrate while the top transparent phase can be removed with a plastic pipette. This washing step is repeated twice before adding a few mL of toluene. The mixture is then centrifuged at 6000 rpm for 4 minutes. The supernatant is discarded while the formed solid pellets of NCs can be re-dispersed in 100 μL of DMF to obtain the ink of HgTe. A few cycles of sonication - vortex - centrifugation can help promote particle dispersion.

Film deposition: A single side polished saphire wafer is cleaned by sonication in an acetone batch. The subtrate is then further clenaed by a flow of acetone and isopropanol before being dried. For uncoupled film we spin coated the solution of nanocrystal in toluene. For uncoupled uncoupled nanocrystals, the pristine solution is directly spin coated on the same substrate For coupled nanocrystals we use the HgTe ink solution. A few drops of DMF are spread on the surface of the patterned sapphire substrate before a spin-coating at 3000 rpm for 30s. This step is necessary to promote the adhesion between the sapphire surface and the NC ink. Then we deposit one drop of the ink solution on the substrate and conduct a two steps spin-coating. First, speed is set at 1500 rpm for 240 s and then the film is dried using a higher speed (2500 rpm) for 60 s. A smooth film of HgTe NCs is formed.

---

† These authors contributed equally to this work.

* Corresponding author: Davide.Boschetto@ensta.fr

II. ELECTRONIC STRUCTURE CALCULATIONS

In order to explain the experimental results, we conducted numerical simulations of HgTe quantum dots to get their energy spectrum and eigenstates so we could calculate the oscillator strength of the different transitions. It helps to figure out which optical transitions are possible. Unless specified otherwise, m stands for the mass of the electron in all the equations.

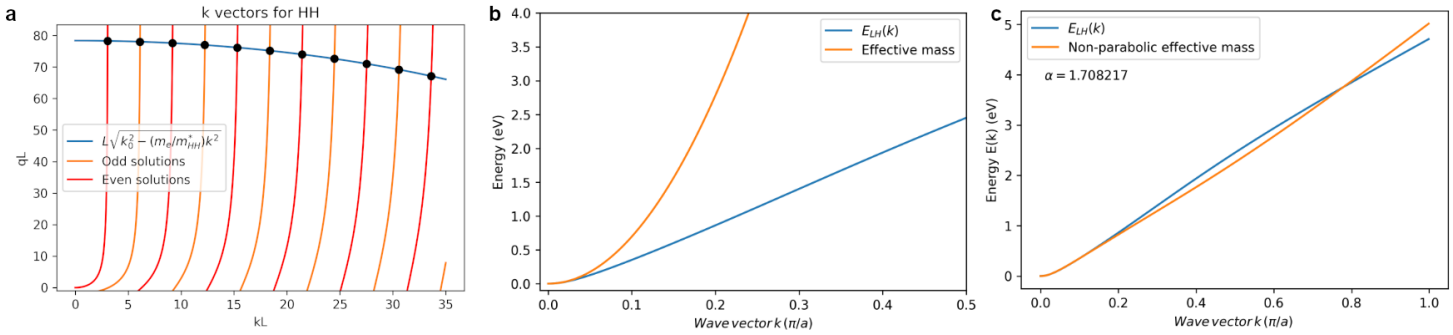

FIG. S1: (a) Geometric resolution for the HH band of HgTe. (b) Comparison of the LH band calculated with the kp 14 bands model (blue) and the parabolic band with an effective mass $m^*_{LH} = 0.013m_e$. (yellow) (c) Comparison with the non-parabolic effective mass approximation.

A. HgTe Quantum dots energy spectrum

As nanocrystals are composed of a finite number of primitive cells compared to bulk crystals, ab initio approaches cannot be advantageously carried in the Fourier space as the domain needed to be considered becomes gigantic and is no longer limited to the first Brillouin zone. A more simple approach, which still provides good first order approximation of the oscillator strengths, is to apply the quantum well model to the bulk bands of the material. By treating the 3 dimensions independently, the energy levels of HgTe quantum dots sample can be retrieved for the energy levels close to the Fermi level by taking into account LH and HH bands as calculated within the k.p 14 bands model of bulk HgTe [1].

1. *Resolution of the one-dimensional Schrodinger equation*

In the simplest QD model, we can consider a cubic quantum dots of side length L and assumed that both bands are isotropic such that the hamiltonian of the system can be separated into three hamiltonians for each direction of space. Therefore, the eigenstates of the hamiltonian are straightforward to calculate [2][3]. For a finite potential height V_0, the geometric solution of the confined states obeys the following conditions:

$$k_0^2 = \frac{m^*_{out}}{m^*_{in}}k_n^2 + q_n^2 \text{ with } k_0^2 = \frac{2m^*_{out}V_0}{\hbar^2} \tag{S1}$$

$$\begin{aligned} q_n &= k_n \tan(k_n L/2) \quad \text{for even solutions} \\ q_n &= -k_n \cot(k_n L/2) \quad \text{for odd solutions} \end{aligned} \tag{S2}$$

From which we deduce the eigenvalues :

$$E_n = \frac{\hbar^2 k_n^2}{2m^*_{in}} \tag{S3}$$

By using equation (S1) and the set of equations (S2), it is possible to find geometrically the solutions of the one-dimensional Schrodinger equation as shown in FigS1.a. Where $m^*_{out} = m_e$ is the electron mass, $m^*_{in} = 0.69m_e$ is the effective mass of the HH band holes in HgTe [1], L is the length of the well and the potential barrier $V_0 = 4.52$ eV. The length parameters used for our model are $L_x = 5.58$ nm, $L_y = 6.25$ nm and $L_z = 15.23$ nm.

2. Band non-parabolicity

The first conduction band of HgTe, the LH band has been shown to be highly non-parabolic [1][4] and the effective mass found for the centre of the Brillouin zone is $m^*_{LH} = 0.013m_e$ [1]. As such, the parabolic approximation is not good enough to predict the energies of the first excited states (see FigS1.b).

In order to tackle this problem, the previous equations are solved by taking into account the effective mass which depends on the energy [2] such as:

$$m^*(E(k)) = m^*(E(0))(1 + \alpha E(k))^{1/3}(1 + 2\alpha E(k))^{2/3} \tag{S4}$$

The fitting parameter α, which equals ≈1.7, is adjusted in order to match the 14 bands kp model as shown in FigS1.c. Accordingly, the geometric resolution of the Schrödinger equation using the equations (S1) and (S2) combined with the fitting of the a parameter for the HH band gives the energies of the confined hole states.

3. Three dimensional system

Following the previous calculations and by treating each spatial variable independently, the eigenvalues of the Schrödinger equation for the quantum dot are computed. All the possible combinations for a set of wave vectors are calculated for the one-dimensional system of each band. For an eigenvector $\left|k_{n_x}, k_{n_y}, k_{n_z}\right\rangle$, we get:

$$E_{n_x,n_y,n_z} = \frac{\hbar^2}{2m^*_{in}}(k^2_{n_x} + k^2_{n_y} + k^2_{n_z}) \tag{S5}$$

From here, we will use the notation $|k\rangle$ with $k^2 = k^2_{n_x} + k^2_{n_y} + k^2_{n_z}$.

B. Oscillator Strength

The oscillator strength is a dimensionless quantity that express the weight of an optical transition.

1. Difference between interband and intraband transitions

In the simple model we are using, the orthogonal eigenfunctions we get are actually envelope functions defined over a single band. So, while we can easily use the equation intraband transitions :

$$f_{intra} = \frac{2}{3m(E_{k'} - E_k)} \sum_{x_i=x,y,z} |\left\langle k'\right| \hat{p_{x_i}} \left|k\right\rangle|^2 \tag{S6}$$

This equation is wrong for interband transitions because those wavefunctions do not take into account the periodicity of the crystal as Bloch functions would. For an interband transition with Bloch functions of the form $\psi_{\nu,\vec{k}}(\vec{r}) = \varphi_{\vec{k}}(\vec{r})u_{\nu,\vec{k}}(\vec{r})$, the extradiagonal terms of the momemtum operator, for a transition from a band v to a band c, are of the form :

$$\left\langle \psi_{c,\vec{k'}} \middle| \hat{\vec{p}} \middle| \psi_{v,\vec{k}} \right\rangle = \int \varphi^*_{\vec{k'}}(\vec{r}) u^*_{c,\vec{k'}}(\vec{r}) \vec{\nabla}(\varphi_{\vec{k}}(\vec{r}) u_{v,\vec{k}}(\vec{r}))\, d^3\vec{r}$$

As the functions $u_{\nu,\vec{k}}(\vec{r})$ are orthogonal and variate much faster than the functions $\varphi_{\vec{k}}(\vec{r})$, we can write :

$$\left\langle \psi_{c,\vec{k'}} \middle| \hat{\vec{p}} \middle| \psi_{v,\vec{k}} \right\rangle = \left\langle \varphi_{\vec{k'}} \middle| \varphi_{\vec{k}} \right\rangle \int u^*_{c,\vec{k'}}(\vec{r}) \vec{\nabla}(u_{v,\vec{k}}(\vec{r}))\, d^3\vec{r} = \left\langle \varphi_{\vec{k'}} \middle| \varphi_{\vec{k}} \right\rangle \vec{p_{cv}} \tag{S7}$$

From equation (S7), the oscillator strength becomes[5] :

$$f_{inter} = \frac{2|p_{cv}|^2}{m(E_{k'} - E_k)} |\left\langle k'|k\right\rangle|^2 \tag{S8}$$

With this model, we were not able to access the Kane momentum p_{cv} so we supposed it was a constant which did not depend on the $\vec{k}$ vector and extracted the value from another publication giving the oscillator strength of the first exciton depending on quantum dot size[6]. We note that it corresponds roughly to the matrix element $P = \sqrt{E_p\hbar^2/(2m_0)}$ with E_p=30 eV as deduced from the 14-band k.p model of reference [1].

C. Density of states and joint density of states

The density of state was computed by using the textbook case of the density of states (DOS) for quantum dots [2] for which Dirac deltas have been replaced by gaussians to take into account the size distribution of the dots. This gives us the following DOS ρ_{QD} for a quantum dot with 2N states of energy E_n :

$$\rho_{QD}(E) = \sum_{n=0}^{N-1} \sqrt{\frac{2}{\pi\sigma_n^2}} e^{-\frac{1}{2}\left(\frac{E-E_n}{\sigma_n}\right)^2} \tag{S9}$$

From there, it was possible to compute the joint density of states (JDOS) ρ_{cv} using the procedure described in reference [7]. The JDOS can be obtained using the following equation:

$$\rho_{cv}(\omega) = \frac{\beta}{2\Omega}(\rho_{QD}^{c} * \rho_{QD}^{v})(\hbar\omega)\delta_{\vec{k_v}\vec{k_c}} \tag{S10}$$

β, Ω, ρ_{QD}^{c}, ρ_{QD}^{v} and $\delta_{\vec{k_v}\vec{k_c}}$ are respectively a normalization constant, the volume of the quantum dot, the conduction DOS, the valence DOS and the kronecker symbol to only allow vertical transitions.

III. RELATIVE CHANGE IN REFLECTIVITY AT A RESONANT TRANSITION

We calculate the change in the real part of the refractive index Δn as a function of the changes in absorption Δk (imaginary part of the refractive index) using the Kramers-Kronig relations, under the simplified approximation that the probe frequency ω matches the energy gap ω_0 (i.e., $\omega = \omega_0$). This will allow us to understand which term dominates in driving the changes in reflectivity.

A. The simplified model

The Kramers-Kronig relations link the real and imaginary parts of a material's complex refractive index $\tilde{n}(\omega) = n(\omega) + ik(\omega)$. Specifically, the change in the real part of the refractive index $\Delta n(\omega)$ due to a change in absorption $\Delta k(\omega')$ is given by:

$$\Delta n(\omega) = \frac{1}{\pi}\,\mathcal{P}\int_{-\infty}^{\infty} \frac{\Delta k(\omega')}{\omega' - \omega}\, d\omega' \tag{S11}$$

where $\mathcal{P}$ denotes the Cauchy principal value of the integral.
Here, we make the following simplifying assumptions:

- **Probe photon frequency matches the energy gap:** $\omega = \omega_0$.
- **Significant Δk near ω_0:** The change in absorption $\Delta k(\omega')$ is significant only near ω_0

To model $\Delta k(\omega')$, we use a Lorentzian function centered at ω_0:

$$\Delta k(\omega') = \Delta k_0 \,\frac{\gamma^2}{(\omega' - \omega_0)^2 + \gamma^2} \tag{S12}$$

where:

- Δk_0 is the peak of the change in absorption.
- γ is the linewidth (damping constant) of the absorption feature.

Substituting the Lorentzian form of $\Delta k(\omega')$ into the Kramers-Kronig relation:

$$\Delta n(\omega) = \frac{1}{\pi}\,\mathcal{P}\int_{-\infty}^{\infty} \frac{\Delta k_0\,\gamma^2}{(\omega' - \omega_0)^2 + \gamma^2} \cdot \frac{1}{\omega' - \omega}\, d\omega' \tag{S13}$$

$$= \Delta k_0 \cdot \left[\frac{\omega - \omega_0}{(\omega - \omega_0)^2 + \gamma^2}\right] \tag{S14}$$

This result uses the standard Hilbert transform of a Lorentzian function.

Setting $\omega = \omega_0$:

$$\Delta n(\omega_0) = \Delta k_0 \cdot \left[\frac{\omega_0 - \omega_0}{(\omega_0 - \omega_0)^2 + \gamma^2} \right] = 0 \tag{S15}$$

Therefore, at the resonance frequency, the change in the real part of the refractive index is zero.

On the other side, the changes in reflectivity ΔR can be expressed as:

$$\Delta R_{\omega_0} = \left(\frac{\partial R}{\partial n} \right)_{\omega_0} \Delta n(\omega_0) + \left(\frac{\partial R}{\partial k} \right)_{\omega_0} \Delta k(\omega_0) \tag{S16}$$

But since $\Delta n(\omega_0) = 0$:

$$\Delta R_{\omega_0} \approx \left(\frac{\partial R}{\partial k} \right)_{\omega_0} \Delta k(\omega_0) \tag{S17}$$

This implies that the reflectivity change ΔR at ω_0 is dominated by $\Delta k(\omega_0)$.

This calculation confirms that, at the band edge, the change in reflectivity is predominantly due to changes in absorption, and the dispersive contribution to the refractive index can be neglected in a first order approximation.

B. Estimation of the numerical values

We estimate $\left(\frac{\partial R}{\partial k} \right)_{\omega_0}$ using $n = 2.3$ and $k = 0.1$ from reference [8].

The reflectivity R at normal incidence is:

$$R = \left| \frac{n - 1 + ik}{n + 1 + ik} \right|^2 = \frac{(n-1)^2 + k^2}{(n+1)^2 + k^2} \tag{S18}$$

whose partial derivative with respect to k is:

$$\frac{\partial R}{\partial k} = \frac{2k \left[(n+1)^2 - (n-1)^2 \right]}{\left[(n+1)^2 + k^2 \right]^2} = \frac{8nk}{\left[(n+1)^2 + k^2 \right]^2} \tag{S19}$$

Using $n = 2.3$ and $k = 0.1$:

$$\frac{\partial R}{\partial k} = \frac{8 \times 2.3 \times 0.1}{\left[(2.3+1)^2 + (0.1)^2 \right]^2} \approx 0.01548 \tag{S20}$$

Therefore:

$$\left(\frac{\partial R}{\partial k} \right)_{\omega_0} \approx 0.01548 \tag{S21}$$

Moreover, we can also calculate the reflectivity R at ω_0:

$$R = \frac{(n-1)^2 + k^2}{(n+1)^2 + k^2} \approx 0.15596 \tag{S22}$$

C. Estimation of the changes in absorption

In a pump-probe experiment involving HgTe quantum dots, the measured relative change in reflectivity is:

$$\frac{\Delta R}{R} = 10^{-3} \tag{S23}$$

From the previous calculations, we have:

$$\Delta R \approx \alpha \Delta k \tag{S24}$$

where α is given by:

$$\alpha = \left(\frac{\partial R}{\partial k}\right)_{\omega_0} \approx 0.01548 \tag{S25}$$

from which we can calculate the absolute change in reflectivity ΔR:

$$\Delta R = R \times \frac{\Delta R}{R} = 1.56 \times 10^{-4} \tag{S26}$$

Using the relationship $\Delta R \approx \alpha \Delta k$, we can solve for Δk:

$$\Delta k = \frac{\Delta R}{\alpha} = \frac{1.56 \times 10^{-4}}{0.01548} \approx 0.01007 \tag{S27}$$

The relative change in k is:

$$\frac{\Delta k}{k} = \frac{0.01007}{0.1} = 0.1007 \tag{S28}$$

which means a significant relative changes of around 10% at $\omega = \omega_0$.

IV. COMPUTATION OF THE AVERAGE NUMBER OF ABSORBED PHOTONS PER QD

In order to calculate the average number of absorbed photons per QD, we need to know the absorption cross section $\sigma(\omega)$ of the film for the pump frequency ω, which is written as :

$$\sigma(\omega) = \frac{2\omega\kappa(\omega)}{cn_{QD}} \tag{S29}$$

κ, c and n_{QD} are the imaginary part of the optical index, the speed of light and the density of quantum dots respectively. The value of the absorption cross section at the absorption edge of HgTe QDs has been documented in the literature and is about $\sigma(\omega_0) \approx 1 \cdot 10^{-15}$ [9]. As c and n_{QD} doesn't depend on the pump frequency, we can determine The imaginary part of the optical index is about 0.1 at the band edge while it is about 0.15 at $\omega_1 = 1.55$ eV (800 nm) [8]. By cross multiplication, we obtain :

$$\sigma(\omega_1) = \frac{\omega_1\kappa(\omega_1)}{\omega_0\kappa(\omega_0)}\sigma(\omega_0) \tag{S30}$$

We finally obtain $\sigma(\omega_1) \sim 3.6 \cdot 10^{-15}$ cm². As an example, for a fluence F of 60 µJ/cm² we get the average number of excitations per QD $\langle N \rangle = \sigma F/\hbar\omega \approx 0.86$ [10]. Previous studies have assumed the generation of excitons per QD followed a Poisson distribution [10, 11]. As such, we calculate it for different number of photons absorbed per QD N :

$$P_N = \frac{\langle N \rangle^N}{N!} e^{-\langle N \rangle} \tag{S31}$$

The Poisson statistics for 0.86 excitations per QD gives about 36% of monoexcited QD and 14% of doubly excited QD. S2 shows the Poisson statistics of the different fluences we used in our experiments.

V. TRANSIENT REFLECTIVITY

Figure S3 compares the transient experimental reflectivity variation between the uncoupled (short dash line) and the coupled (full line) samples. The scale is the same for both considered low and high energy 2.2 and 1.2 wavelengths and for both samples. The relaxation at short times below 5 ps is clearly faster for the coupled QDs than for the uncoupled QDs. The measurements also show that the high energy reflectivity variation amplitude at 1.2 μm wavelength is much smaller than the low energy one at 2.2 μm wavelength (note the broken vertical scale), as a result likely of a transient strong photo-induced absorption compensating the interband absorption bleaching. We attribute this photo-induced absorption to an intraband absorption between the P-like conduction states to the D-like one, expected to exhibit a strong intraband dipole.

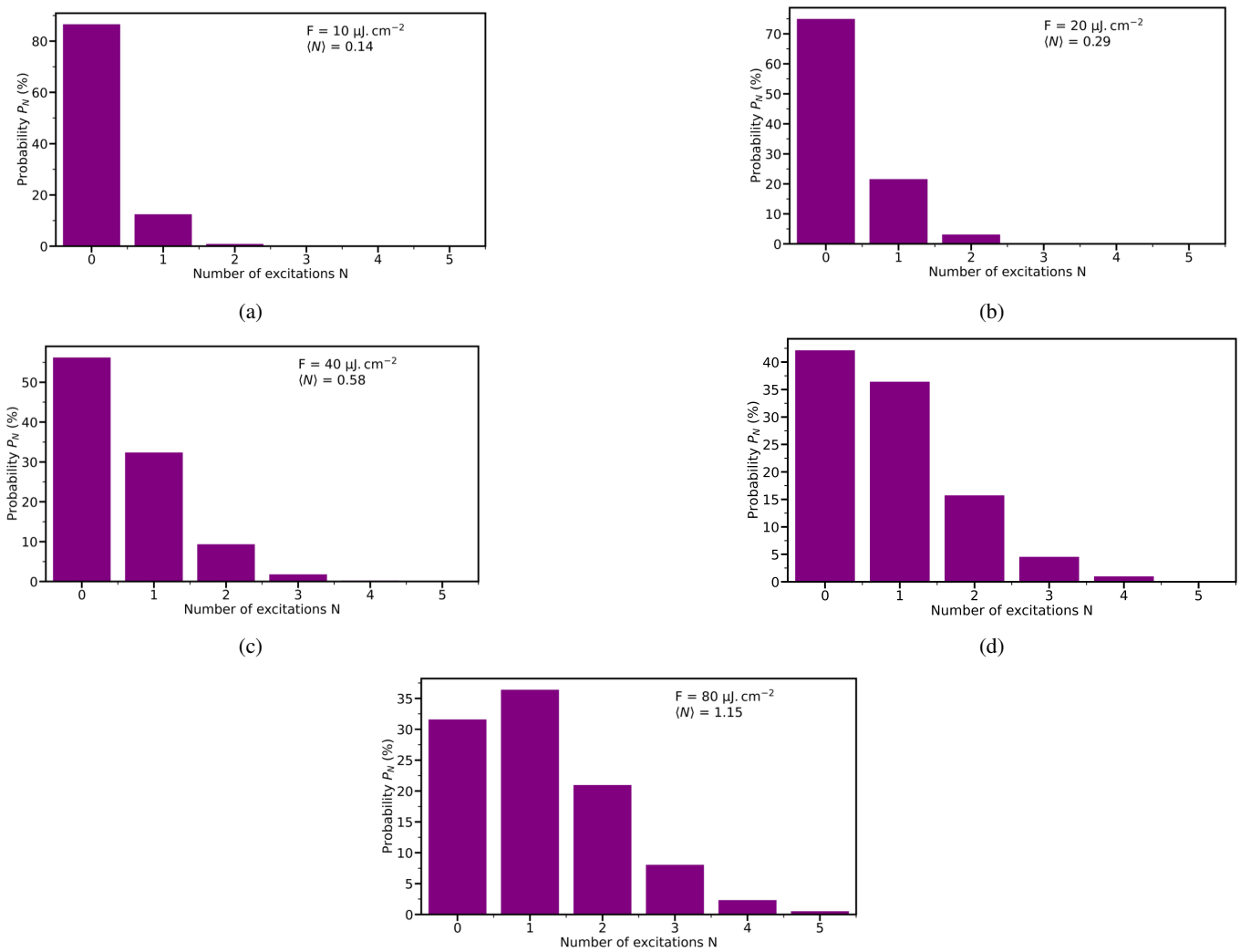

FIG. S2: Poisson distribution of excitations for several fluences between 10 and 80 $\mu\mathrm{J/cm^2}$. (a) 10 $\mu\mathrm{J/cm^2}$. (b) 20 $\mu\mathrm{J/cm^2}$. (c) 40 $\mu\mathrm{J/cm^2}$. (d) 60 $\mu\mathrm{J/cm^2}$. (e) 80 $\mu\mathrm{J/cm^2}$.

VI. MODELLING OF THE ELECTRON AND HOLE DYNAMICS

The rate equation model is written on the populations of electrons and holes averaged over the nanocrystal ensemble. The model considers 3 different mechanisms:

- intraband relaxation,
- interband Sh-Se recombination,
- multiparticle Auger recombination.

Intraband relaxation from level i to level j $(1 \leq i, j \leq 3)$ is written with the two following contributions to the population rates on the initial i and final j states:

$$\frac{dN_i}{dt} = -\frac{N_i(t)}{\tau_{ij}} \quad \text{and} \quad \frac{dN_j}{dt} = +\frac{N_i(t)}{\tau_{ij}}$$

where τ_{ij} is the relaxation time from level i to level j. To account for the Pauli exclusion principle for the pseudo-levels N_{e1}

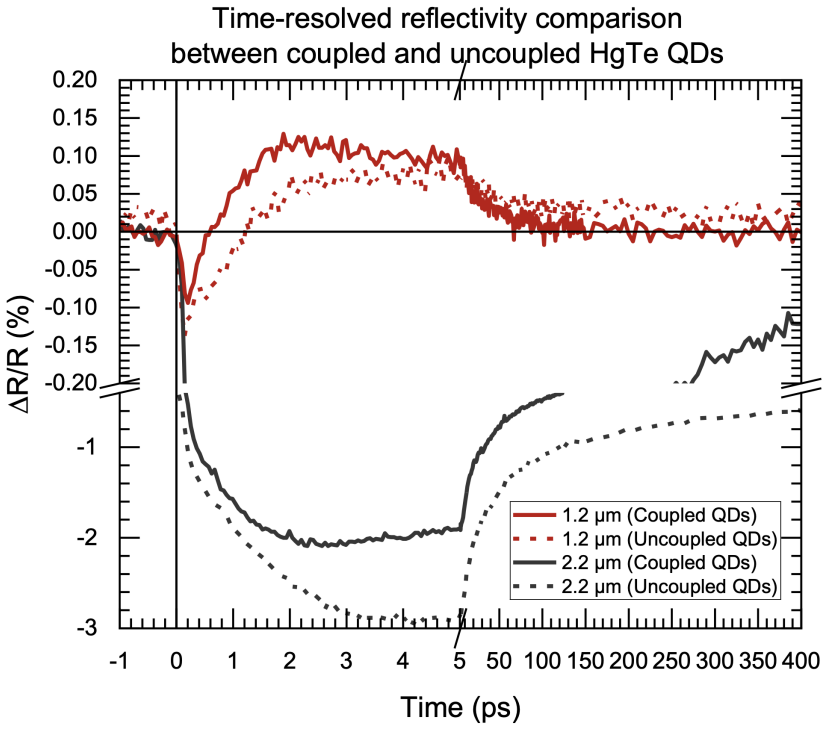

FIG. S3: Comparison between the experimental transient reflectivity variation in the sample of uncoupled (dashed line) and coupled (full line) quantum dots.

and N_{h1} with a degeneracy of only 2, the model includes the occupation factor of the relaxation towards these two levels:

$$\frac{dN_j}{dt} = +\frac{(1 - N_j/2)N_i(t)}{\tau_{ij}}.$$

To account for the interband recombination, the model only considers the recombination from the N_{e1} and N_{h1} pseudo-levels, since the other levels undergo much faster relaxation. The following form

$$\frac{dN_{e1,h1}}{dt} = -\frac{\sqrt{N_{e1}(t)N_{h1}(t)}}{\tau_{\text{exc}}}$$

corresponds to a monoexponential decay of the electron and hole ground state population with recombination time τ_{exc} and preserves the equality of the total number of electrons to the total number of holes, as shown in Figure S5.

At last, the model includes an Auger three-particle collision mechanism as described in Figure 5 (b) in the main text, with a trimolecular coefficient $1/\tau_{\text{Auger}}$ ensuring the recombination of an electron-hole pair occupying the ground level and the promotion of the second electron towards the N_{e2} pseudo-level.

Figure S4 compares the experimental reflectivity and the calculated transient differential absorption in a non-normalized linear scale (on the left) and in log scale (on the right) considering the absolute values of the quantities in this later case. The biexponential exciton recombination is clearly apparent in the transient absorption of the model and roughly in the experimental data supporting the presence of a three-particle Auger recombination mechanism.

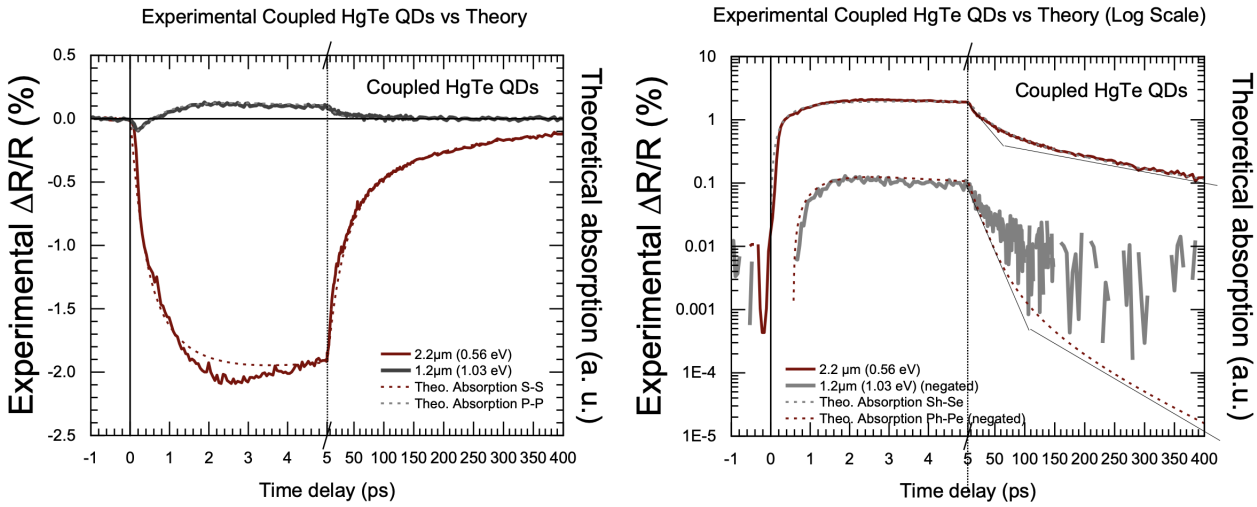

FIG. S4: Transient reflectivity change in a log scale for the coupled sample at 1.2 μm wavelength (black full line) and at 2.2 μm wavelength (red full line) and corresponding transient absorption as calculated by the dynamics rate equation model (dashed line), represented in vertical linear scale (left) and log scale (right). In the log scale, the absolute value of the reflectivity change is considered. The scales are the same and comparable experimentally for both wavelengths (no normalization) and theoretically for the $S_h - S_e$ and $P_h - P_e$ calculated absorption (same scale). The thin lines in log scale are guides to the eyes for the bi-exponential exciton recombination in the dynamics model.

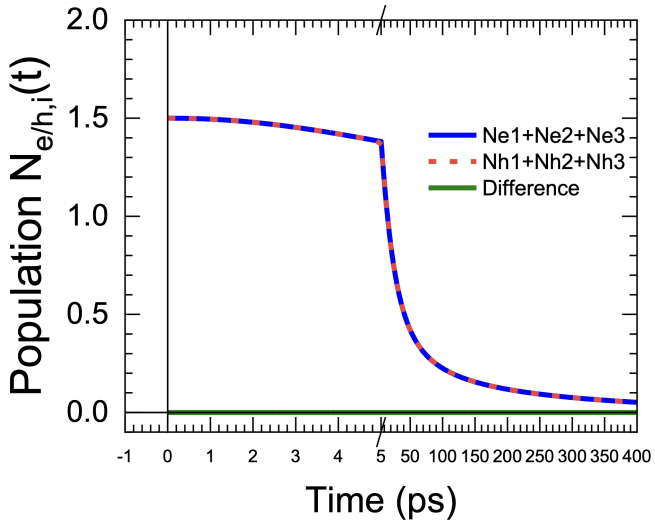

FIG. S5: Total number of electrons (full line) and holes (dashed line) as a function of time as calculated by the rate equation model. The difference (green full line) is zero at all times.

VII. EXPERIMENTAL REFLECTIVITY MEASUREMENTS WITHOUT NORMALIZATION

Figure S6 and S7 show the transient reflectivity for both uncoupled and coupled HgTe QDs, respectively, without normalization, at a pump fluence of 60 μJ/cm^2.

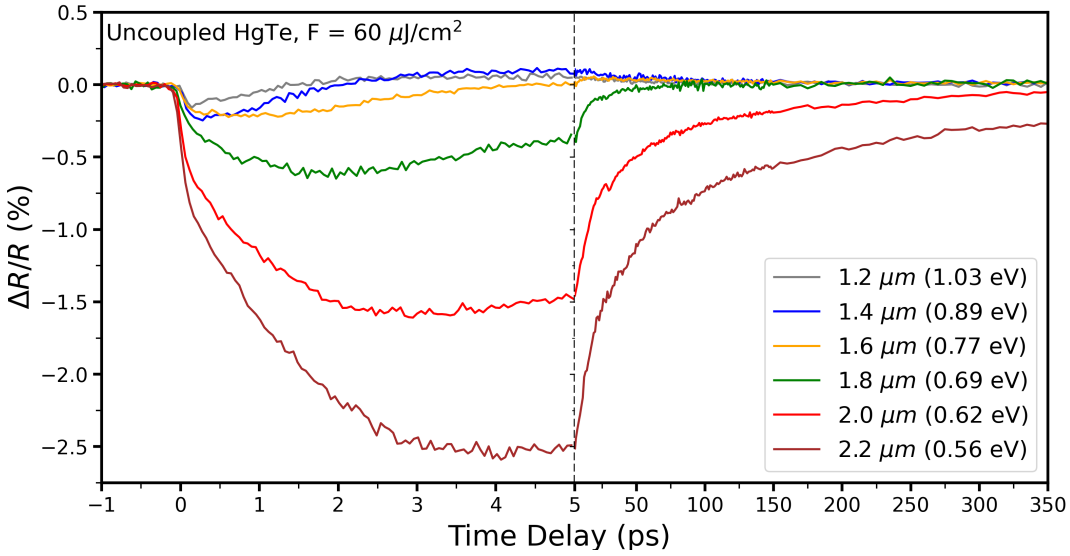

FIG. S6: Transient reflectivity versus pump-probe time delay without normalization for uncoupled HgTe QDs, at a pump fluence of 60 μJ/cm^2.

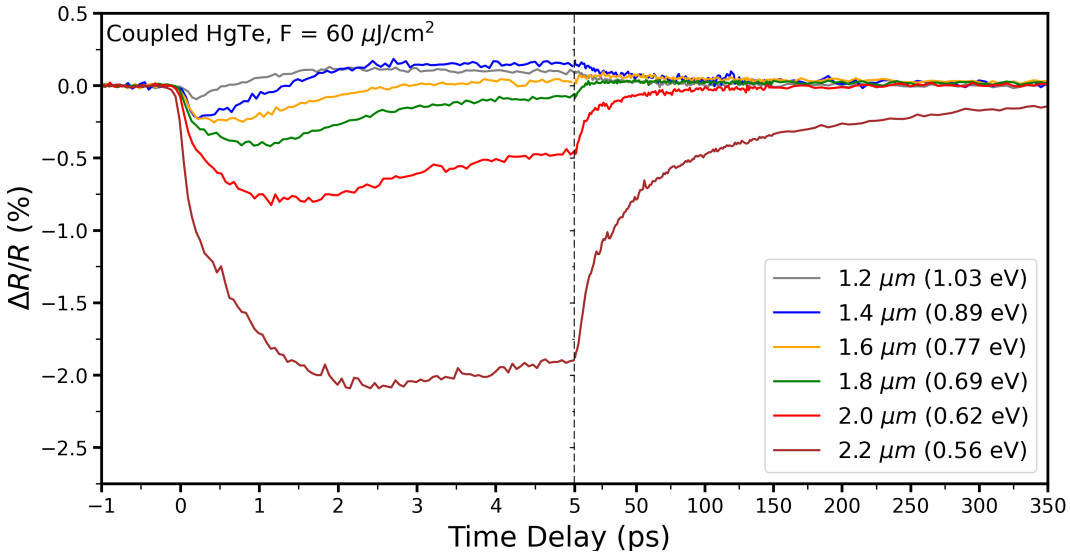

FIG. S7: Transient reflectivity versus pump-probe time delay without normalization for coupled HgTe QDs, at a pump fluence of 60 μJ/cm^2.

VIII. BIBLIOGRAPHY

[1] N. Moghaddam, C. Gréboval, J. Qu, A. Chu, P. Rastogi, C. Livache, A. Khalili, X. Z. Xu, B. Baptiste, S. Klotz, G. Fishman, F. Capitani, S. Ithurria, S. Sauvage, and E. Lhuillier, "The Strong Confinement Regime in HgTe Two-Dimensional Nanoplatelets," *The Journal of Physical Chemistry C*, vol. 124, pp. 23460–23468, Oct. 2020.

[2] P. Harrison and A. Valavanis, *Quantum wells, wires and dots: theoretical and computational physics of semiconductor nanostructures*. Chichester, West Sussex, United Kingdom ; Hoboken, NJ, USA: Wiley, fourth edition ed., 2016.

[3] C. Cohen-Tannoudji, B. Diu, and F. Laloë, *Mécanique quantique - Tome I*. Savoirs actuels, Les Ulis Paris: EDP sciences CNRS éditions, nouvelle éd ed., 2018.

[4] G. Allan and C. Delerue, "Tight-binding calculations of the optical properties of HgTe nanocrystals," *Physical Review B*, vol. 86, p. 165437, Oct. 2012.

[5] B. Alén, J. Bosch, D. Granados, J. Martínez-Pastor, J. M. García, and L. González, "Oscillator strength reduction induced by external electric fields in self-assembled quantum dots and rings," *Physical Review B*, vol. 75, p. 045319, Jan. 2007.

[6] E. Lhuillier, S. Keuleyan, and P. Guyot-Sionnest, "Optical properties of HgTe colloidal quantum dots," *Nanotechnology*, vol. 23, p. 175705, May 2012.

[7] C. Cabrera, D. Contreras-Solorio, and L. Hernández, "Joint density of states in low dimensional semiconductors," *Physica E: Low-dimensional Systems and Nanostructures*, vol. 76, pp. 103–108, Feb. 2016.

[8] P. Rastogi, A. Chu, T. H. Dang, Y. Prado, C. Gréboval, J. Qu, C. Dabard, A. Khalili, E. Dandeu, B. Fix, X. Z. Xu, S. Ithurria, G. Vincent, B. Gallas, and E. Lhuillier, "Complex Optical Index of HgTe Nanocrystal Infrared Thin Films and Its Use for Short Wave Infrared Photodiode Design," *Advanced Optical Materials*, vol. 9, p. 2002066, May 2021.

[9] J. Qu, M. Weis, E. Izquierdo, S. G. Mizrahi, A. Chu, C. Dabard, C. Gréboval, E. Bossavit, Y. Prado, E. Péronne, S. Ithurria, G. Patriarche, M. G. Silly, G. Vincent, D. Boschetto, and E. Lhuillier, "Electroluminescence from nanocrystals above 2 μm," *Nature Photonics*, vol. 16, pp. 38–44, Jan. 2022.

[10] A. Al-Otaify, S. V. Kershaw, S. Gupta, A. L. Rogach, G. Allan, C. Delerue, and D. J. Binks, "Multiple exciton generation and ultrafast exciton dynamics in HgTe colloidal quantum dots," *Physical Chemistry Chemical Physics*, vol. 15, no. 39, p. 16864, 2013.

[11] V. I. Klimov, J. A. McGuire, R. D. Schaller, and V. I. Rupasov, "Scaling of multiexciton lifetimes in semiconductor nanocrystals," *Physical Review B*, vol. 77, p. 195324, May 2008.